



Open Archive TOULOUSE Archive Ouverte (OATAO)

OATAO is an open access repository that collects the work of Toulouse researchers and makes it freely available over the web where possible.

This is an author-deposited version published in : <http://oatao.univ-toulouse.fr/>
Eprints ID : 14014

To link to this article : doi: 10.1179/1743133613Y.0000000095
URL : <http://dx.doi.org/10.1179/1743133613Y.0000000095>

To cite this version : Escobar, A. and Celentano, D. and Cruchaga, Marcela and Lacaze, Jacques and Schulz, Bernd and Dardati, P. and Parada, Antonio *Experimental and numerical analysis of effect of cooling rate on thermal–microstructural response of spheroidal graphite cast iron solidification*. (2014) *International Journal of Cast Metals Research*, vol. 27 (n° 3). pp. 176-186. ISSN 1364-0461

Any correspondence concerning this service should be sent to the repository administrator: staff-oatao@listes-diff.inp-toulouse.fr

Experimental and numerical analysis of effect of cooling rate on thermal–microstructural response of spheroidal graphite cast iron solidification

A. Escobar¹, D. Celentano*², M. Cruchaga³, J. Lacaze⁴, B. Schulz¹, P. Dardati⁵ and A. Parada¹

This work presents an experimental and numerical study of the solidification process of an eutectic spheroidal graphite cast iron (SGI). The effect of the cooling rate on the thermal–microstructural response is particularly analysed. To this end, experiments as well as numerical simulations were carried out. The experiments consisted in a solidification test in a wedge-like casting such that different cooling rates were measured at specific positions along the part. A metallographic analysis was also performed in five locations of the sample with the aim of obtaining the number and size of graphite nodules at the end of the process. The numerical simulations were made using multinodular based and uninodular based models. These two models predicted similar results in terms of cooling curves and nodule counts. Besides, good experimental–numerical agreements were obtained for both the cooling curves and the graphite nodule counts.

Keywords: Spheroidal graphite cast iron, Solidification, Microstructure, Numerical simulation, Cooling rate, Finite elements

Introduction

Spheroidal graphite cast iron (SGI), also known as ductile iron or nodular cast iron was first developed in 1949 by Keith Dwight Millis¹ using a Mg–Cu alloy as spheroidising agent. Some of the well known properties making SGI an attractive material are: versatility, good performance/cost ratio, high corrosion and wear resistance, ductility and high tensile resistance. In particular, the automotive industry has shown a great interest and trust in this material through the use of this material in safety components such as steering knuckles and calipers.² Another critical application that reflects the confidence put in this material is the storing and transport of nuclear waste.¹

The microstructure of nodular cast iron, depending on the cooling conditions (undercooling) and the presence of alloying elements in the melt, can consist in ferrite,

martensite, pearlite, ausferrite, retained austenite, bainite and spheroidal graphite homogeneously distributed in the matrix.³ This microstructure is the responsible for the good properties of this material and the main reason of the many studies devoted to it since its appearance. The asymmetric coupled phase diagrams which describes non-equilibrium solidification is one of the most important concepts in understanding the variation of microstructures that can occur during solidification of cast iron. The theoretical construction of these diagrams was reviewed by Lux *et al.*⁴ and also documented by Jones and Kurz.⁵ Through this understanding, a better control on the physical properties of the final product could be obtained. One of the most important parameters on the microstructure control of SGI is the cooling rate. High cooling rates produce large amounts of carbides in the matrix, causing a decrease in ductility and toughness of the material and requiring expensive heat treatments for the dissolution of such carbides.

In the cooling process of an eutectic nodular cast iron, the nucleation of the austenite–graphite eutectic starts once the temperature reaches the equilibrium eutectic temperature. It is widely accepted that the growth kinetics of nodular cast iron is primarily controlled by solid state diffusion of carbon through the austenite shell.^{6,7} Two models based on either deterministic laws or stochastic procedures describe the growth mechanism and the solidification process of eutectic nodular cast iron: uninodular^{7–16} and multinodular^{17–21} models. The former considers that spherical graphite nuclei are immediately enveloped by an austenite shell

¹Departamento de Ingeniería Metalúrgica, Universidad de Santiago de Chile (USACH), Av. Bernardo O'Higgins 3363, Santiago, Chile

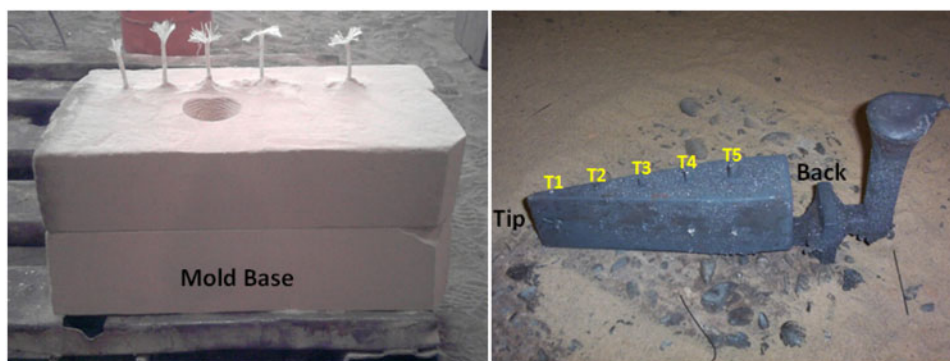
²Departamento de Ingeniería Mecánica y Metalúrgica, Pontificia Universidad Católica de Chile (PUC), Av. Vicuña Mackenna 4860, Santiago, Chile

³Departamento de Ingeniería Mecánica, Universidad de Santiago de Chile (USACH), Av. Bernardo O'Higgins 3363, Santiago, Chile

⁴Centre Interuniversitaire de Recherche et d'Ingénierie des Matériaux (CIRIMAT), Ecole Nationale Supérieure des Ingénieurs en Arts Chimiques Et Technologiques (ENSIACET), BP 44362, 31030 Toulouse cedex 4, France

⁵Departamento de Ingeniería Mecánica – CIII, Facultad Regional Córdoba, Universidad Tecnológica Nacional, M. López y Cruz Roja Argentina, Córdoba, Argentina

*Corresponding author, email dcelentano@ing.puc.cl



1 Wedge-like casting used in present study showing temperature measurement locations (T1–T5)

and subsequent growth occurs by carbon diffusion through this envelope. The latter considers that austenite and graphite nucleate independently in the liquid (austenite growing in a dendritic shape and graphite in a spherical shape) and that at some moment (experimentally determined by Boeri¹⁸) graphite is enveloped by the thinnest arms of dendritic austenite and, again, subsequent growth proceeds by carbon diffusion through this phase.

Dardati *et al.*²⁰ compared one model based on the uninodular theory by Su *et al.*⁷ and two models based on the multinodular theory presented in Boeri¹⁸ and Dardati *et al.*²¹ In terms of nodule count the three models showed very similar results with each other and showed a good agreement with the experimental ones. Regarding the cooling curves, the slope of the model developed by Dardati *et al.*²¹ differs from the experimental one during the first cooling stage and also shows the smallest undercooling compared with the other two models and with the experimental one. On the whole, the model by Boeri¹⁸ gave the best fit between numerical and experimental data.

It appeared challenging to compare the multinodular model by Boeri¹⁸ to the uninodular model developed by Lesoult *et al.*^{8,9} which is more elaborated than the early model by Su *et al.*⁷ These models were thus implemented in a micro-macroscopic code. At a macrolevel, the heat equation is solved using the finite element method, whereas the solidification process at the microlevel is modelled using rules for nucleation and growth. The objective of this work is to be able of numerically analysing and comparing the experimental results obtained in a solidification test of a SGI with eutectic composition cast in a wedge-like mould. For this purpose multinodular and uninodular models were implemented. A wedge-like mould was used for this purpose, in which different cooling rates are obtained according to the different thicknesses of the mould. The discussion, comparison and experimental validation of the numerical results provided by these two models encompasses cooling curves and graphite nodule distributions at different positions of the sample.

Experimental

A series of castings were carried out in order to study the effect of cooling rate on the temperature–time cooling curves and on the as cast microstructures. The experiments were carried out in the manufacturing line of a casting industry operating under standard conditions with an induction furnace. Owing to technical issues only one experiment was considered to carry out the validation of the numerical simulations. In this context, although the total weight of metal prepared for the cast was that of the furnace capacity, i.e. 535 kg, the total weight of metal actually used for the test was only 25 kg.

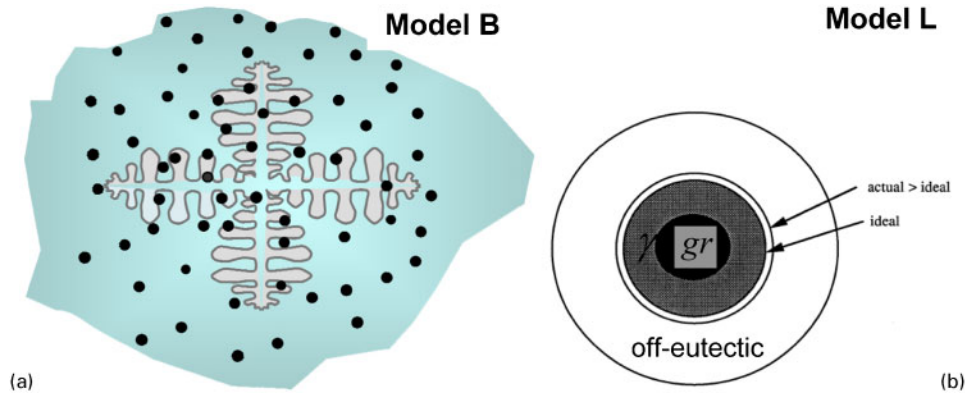
The charge for preparing the melt was made of 46% steel scrap, 51% foundry returns, 2% graphite and 1%Fe–75%Si. The chemical composition of the performed test is summarised in Table 1.

The pouring temperature of the melt was the one commonly used in the foundry, and it led to a maximum recorded temperature of the melt in the mould of $1200 \pm 5^\circ\text{C}$. This temperature will then be used as the filling temperature for the calculations. The morphology of the wedge-like part and the mould used to perform the solidification experiences are shown in Fig. 1. The dimensions of both parts are summarised in Table 2. For the mould, only the base dimensions are presented since the cover has the same values. The temperature of several points (T1–T5) at the centre of the wedge was measured with a K-type thermocouple and recorded by a data acquisition system.

To analyse and validate the results obtained in the performed test, detailed metallographic studies were carried out. In order to experimentally study the size and distribution of the graphite particles in the matrix, the nodule count was obtained with the software Image-Pro Plus and considering the minimum and maximum nodule sizes (nodule radius) in all the locations. These were found to be 5 and 35 μm respectively. The nodule sizes were grouped in classes of 6 μm range, considering the nodule radius (R), thus obtaining five classes. The nodule count in each class is obtained using equation (1). Because of the possibility that automatic analyses accounted for small details which were not

Table 1 Average chemical composition (main elements) of samples/wt-%

| C | Si | Mn | S | P | Mo | Ni | Cu | Al | Cr | Mg | CE |
|------|------|------|-------|-------|------|------|------|-------|------|-------|------|
| 3.39 | 2.67 | 0.52 | 0.047 | 0.053 | 0.01 | 0.02 | 0.01 | 0.001 | 0.08 | 0.042 | 4.28 |



2 Representation of multinodular (Model B, Boeri¹⁸) and uninodular (Model L, Lesoult *et al.*^{9,10}) theories

nodules (porosities, inclusions) and because the graphite fraction related to the small nodules is anyway low, it was decided not to take into account the part of the distributions corresponding to sizes less than the minimum mentioned above.

Different approaches have been proposed to obtain the volume distribution of nodules (N_V), e.g. the correlation by Owadano *et al.*²⁵ is more useful when calculating the overall nodule count while in case of castings with many small nodules the finite difference method by Basak and Sengupta²⁶ should be used. Alternatively, equating the surface and volume fractions the expression that was used in the present work is given by²⁰

$$N_V = \frac{3}{4R} N_A \quad (1)$$

The results obtained with equation (1) are summarised in Table 3. Despite the experimental value of N_V in location T3 (middle location), it is seen that as cooling rate increases the number of nodules per unit volume increases as well. In this table is also presented the experimental solidification time with the aim of giving us a better understanding of the cooling rate effect in each location of the wedge. It is appreciated that as wall thickness increases the total solidification time (T_F) increases as well.

Numerical modelling

Thermal model

To account for phase changes during the cooling process, the well known energy equation may be used

$$\rho c \dot{T} + \rho L \dot{f}_{pc} = \nabla(k \nabla T) \quad (2)$$

Table 2 Wedge-like part and mould dimensions

| Part | Height/mm | Length/mm | Width/mm |
|------------|-----------|-----------|--------------------|
| Wedge | 50 | 400 | Tip: 5 Back: 60 |
| Mould base | 75 | 565 | 250 |

Table 3 Experimental and numerical nodule counts at locations T1–T5

| Location | Wall thickness/mm | N_A experimental/ m^{-2} | N_V experimental/ m^{-3} | T_F experimental/s |
|----------|-------------------|------------------------------|------------------------------|----------------------|
| T1 | 10 | 2.20×10^8 | 2.29×10^{13} | 56.2 |
| T2 | 20 | 1.44×10^8 | 8.75×10^{12} | 178.3 |
| T3 | 30 | 1.56×10^8 | 1.02×10^{13} | 252.3 |
| T4 | 40 | 1.18×10^8 | 8.86×10^{12} | 354.2 |
| T5 | 50 | 1.42×10^8 | 8.58×10^{12} | 375.9 |

where ρ is the density, c is the specific heat, k is the thermal conductivity, T is the temperature, L is the latent heat of phase change, f_{pc} is the phase change function ($0 < f_{pc} < 1$) considered here as the liquid fraction f_l , ∇ is the gradient operator and a dot on the top of a variable indicates time derivative. The solution of this equation must be achieved together with initial and boundary conditions. Equation (2) represents a nonlinear problem, on account of the changes that take place in material parameters with temperature evolution. The solution is carried out by means of a space discretisation using the finite element method and a time discretisation using the finite difference method.^{28,29}

The coupling of the macro and micro problems is made within the same time and domain discretisation. As time is increased the results of the macro solution are transferred to the micro level, which is solved and returns the relevant parameters to the macro level before a new time increment is allowed.

Microstructural model

The first model used in this work is based on the multinodular theory of nucleation and growth of austenite and graphite, work started first by Boeri.¹⁸ Such model, called B from here onward, considers that initially austenite and graphite nucleate in the liquid phase, austenite growing in a dendritic shape, and after a while (when the nodule reaches 6 μm in size, experimentally determined by Boeri¹⁸) graphite is enveloped by the thinnest arms of austenite; see Fig. 2a. The subsequent growth occurs by carbon diffusion through the austenite shell. In order to compare and study the numerical results obtained with this model, a second uninodular based model developed by Lesoult *et al.*^{9,10} taking into account the work by Oldfield²² but modifying the balances of carbon at the interfaces, was considered. There are two versions of this model, called L from now onward, and the one used here assumes all austenite formed during the eutectic reaction deposits as an envelope around the graphite nodules. Furthermore, it assumes that new graphite spheroids get immediately

Table 4 Equations of microstructural models used in simulations

| Model B | Model L |
|--|---|
| Equilibrium parameters | |
| $C^{l/\gamma} = \frac{1}{97.3}(1576 - T - 22.38\text{Si})$ (3) | |
| $C^{\gamma/l} = \frac{1}{177.9}(1528.4 - T - 32.02\text{Si})$ (4) | |
| $C^{l/gr} = \frac{1}{389.1}(T - 112.84\text{Si} + 534.5)$ (5) | |
| $C^{\gamma/gr} = \frac{(T - 1153.7 - 4.865\text{Si})(1.51 - 0.21\text{Si})}{(353.7 + 4.865\text{Si})} 2 + 2.11 - 0.21\text{Si}$ (6) | |
| $T_E = 1153.7 + 4.865 \text{ Si}$ (7) | |
| $C_{TE} = 2.11 - 0.21 \text{ Si}$ (8) | |
| $C_E = 4.34 - 0.28 \text{ Si}$ (9) | |
| Scheil's equation | |
| $\text{Si} = \text{Si}_0(1 - f_s)^{k_{\text{Si}} - 1}$ (10) | |
| Graphite nodules nucleation | |
| $\dot{N} = (1 - f_s)b\Delta T \exp\left(-\frac{c}{\Delta T}\right)$ (11) | |
| Graphite nodules growth | |
| $\dot{r}^{\text{gr}} = \frac{1}{2r^{\text{gr}}} \frac{C^{l/\gamma} - C^{l/gr}}{C^{\text{gr}} - C^{l/gr}} \frac{\rho^l}{\rho^{\text{gr}}} D_C^l$ | $\dot{r}^{\text{gr}} = \frac{r^\gamma}{r^{\text{gr}}} \frac{C^{\gamma/l} - C^{\gamma/gr}}{C^{\text{gr}} - C^{\gamma/gr}} \frac{\rho^\gamma}{\rho^{\text{gr}}} D_C^\gamma$ (12b) |
| for $r_{\text{gr}} \leq 6 \mu\text{m}$ (12a-1) | |
| $\dot{r}^{\text{gr}} = \frac{0.9}{r^{\text{gr}}} \frac{r^\gamma}{\left(\frac{r^\gamma}{r^{\text{gr}}} - 1\right)} \left(\frac{C^{\gamma/l} - C^{\gamma/gr}}{C^{\text{gr}} - C^{\gamma/gr}}\right) \frac{\rho^\gamma}{\rho^{\text{gr}}} D_C^\gamma (1 - f_s)^{2/3}$ | |
| for $r_{\text{gr}} > 6 \mu\text{m}$ (12a-2) | |
| Austenite growth | |
| Growth given by the lever rule (see below for f_γ) | |
| | $\dot{r}^\gamma = \frac{1}{\left(\frac{r^\gamma}{r^{\text{gr}}} - 1\right) f_\gamma} \left(\frac{C^{\gamma/l} - C^{\gamma/gr}}{C^{l/\gamma} - C^{\gamma/l}}\right) \left[1 + \left(\frac{\rho^\gamma}{\rho^{\text{gr}}} - 1\right) \left(\frac{C^{l/\gamma} - C^{\gamma/l}}{C^{\text{gr}} - C^{\gamma/gr}}\right)\right] D_C^\gamma$ (13) |
| Graphite fraction | |
| $f_{\text{gr}} = \sum_1^k \frac{4}{3} \pi N_k (r_k^{\text{gr}})^3$ (14) | |
| Austenite fraction | |
| $f_\gamma = \frac{100 - C_E}{C_E - C_{TE}} f_{\text{gr}}$ (15a) | $f_\gamma = \sum_1^k \frac{4}{3} \pi N_k \left[(r_k^\gamma)^3 - (r_k^{\text{gr}})^3 \right]$ (15b) |
| Solid fraction | |
| $f_s = f_{\text{gr}} + f_\gamma$ (16) | |

surrounded by austenite. The growth unit cell is composed by the graphite nodule enveloped by an austenite shell and the subsequent growth (as temperature decreases) occurs by the carbon diffusion through this envelope (see Fig. 2b). Both models do not consider the existence of a barrier for austenite nucleation and model B takes into account that the quantity of austenite is given by the lever rule for carbon. The equations used by these two models and the correlations used in every case are listed in Table 4.

The parameters $C^{l/\gamma}$, $C^{\gamma/l}$, $C^{l/gr}$ and $C^{\gamma/gr}$, equations (3)–(6), are the equilibrium carbon concentrations at temperature T , of the liquid in equilibrium with austenite, austenite in equilibrium with liquid, liquid in equilibrium with graphite and austenite in equilibrium with graphite respectively. For both models these correlations are the one obtained and developed by Heine.²⁷ In equations (7)–(9),²⁷ T_E , C_{TE} and C_E are the eutectic temperature, the carbon solubility in austenite at the eutectic temperature and the eutectic carbon content respectively. The undercooling is defined as $\Delta T = T_E - T$. Moreover, Si is the silicon content taken into account by the Scheil's equation (equation (10)) with Si_0 the nominal silicon content.

In equation (11), parameters b and c remain constant for a given composition and liquid treatment. The factor $1 - f_s = f_l$, f_l being the liquid fraction, is considered here to

take into account the continuous disappearance of the nucleation sites with the liquid consumption. In this stage it must be clarified that both models consider that nucleation stops when recalescence occurs and starts again when the temperature falls below the last maximum undercooling while solidification is still not completed ($f_s < 1$).

Model B considers the fact that initially the graphite nodules grow in contact with liquid. This growth, expressed by equation (12a-1), is given by Zener equation for the growth of an isolated spherical particle in a matrix with low supersaturation.¹⁸ Here r^{gr} is the graphite radius, ρ^l is the liquid density, ρ^{gr} is the graphite density and D_C^l is the diffusion coefficient of carbon in liquid. After this initial stage of growing in contact with liquid, graphite nodules are assumed in model B to be enveloped by austenite. From this time on the growth rate of the graphite nodules is given by equation (12a-2), where ρ^γ is the austenite density and D_C^γ is the diffusion coefficient of carbon in austenite. In this last equation, a value of 1.89 is considered for the average austenite/graphite radius ratio as considered by Boeri.¹⁸ On the other hand, model L assumes growth rules for the graphite and austenite given by equations (12b) and (13) respectively. In these equations, an asymptotic value of 2.40 is considered for the average austenite/graphite radius ratio.⁶ In equation (14), k

Table 5 Thermal–microstructural properties of SGI²⁰

| Conductivity/W m ⁻¹ °C ⁻¹ | | Specific heat/kJ kg ⁻¹ °C ⁻¹ | | | |
|--|-------|--|-------|---------------------------------|-------|
| Temperature | Value | Temperature | Value | Temperature | Value |
| 280 | 44.1 | 840 | 28.1 | 20 | 500 |
| 420 | 40.9 | 900 | 22.5 | 600 | 750 |
| 560 | 37.1 | 1120 | 18.8 | 800 | 750 |
| 700 | 33.6 | 1400 | 65.0 | 1145 | 820 |
| | | | | 1155 | 840 |
| | | | | 1400 | 840 |
| Density/kg m ⁻³ | | | | 7000 | |
| Latent heat/kJ kg ⁻¹ | | | | 230 | |
| Diffusion coefficients of C/m ² s ⁻¹ | | | | $D_{C^l} = 5.0 \times 10^{-10}$ | |
| Graphite nucleation parameters/m ² s ⁻¹ | | | | $D_{C^r} = 9.0 \times 10^{-11}$ | |
| | | | | $b = 4.0 \times 10^{12}$ | |
| | | | | $c = 400$ | |
| Initial radius of graphite nodules | | | | 1 μm | |
| Initial radius of austenite | | | | 1.2 μm | |
| Density ratios $\frac{\rho^l}{\rho^{gr}} = \frac{\rho^r}{\rho^{gr}}$ | | | | 3.64 | |
| Silicon partition coefficient | | | | 1.09 | |

Table 6 Thermal properties of sand mould²⁰

| Conductivity/W m ⁻¹ °C ⁻¹ | | Density/kg m ⁻³ | | Specific heat/kJ kg ⁻¹ °C ⁻¹ | |
|---|-------|----------------------------|-------|--|-------|
| Temperature | Value | Temperature | Value | Temperature | Value |
| 100 | 0.478 | 100 | 1500 | 100 | 1045 |
| 500 | 0.511 | 500 | | 500 | 1143 |
| 900 | 0.547 | 900 | | 900 | 1238 |
| 1200 | 0.805 | 1200 | | 1200 | 1309 |
| 1400 | 1.194 | 1400 | | 1400 | 1356 |

stands for the number of different nodule radii that are present in a volume element due to the non-simultaneity of nucleation.

The thermal–microstructural properties of the cast iron used in the present analysis are presented in Table 5. The thermal properties of the sand mould and of the different interfaces are respectively given in Tables 6 and 7.

The high value for the heat transfer coefficient at the casting/mould interface was chosen to better fit the experimental and numerical results. Nevertheless, the values presented in the literature are not very different from the one used in the present work. For example, in Ref. 20 the value 1000 is used for this coefficient.

Results and discussion

Models assessment

A 1D simple case numerical simulation was performed for this purpose. This was carried out using a one-element configuration in which the cooling curve, time evolution and final nodule count, Si segregation and liquid fraction evolution were calculated for that element. These results are shown in Fig. 3. As can be seen in this figure both models show similar tendencies when comparing the cooling process. The eutectic

reaction predicted with model B occurs at a little higher temperature than the one predicted by model L, the difference being approximately 5°C thus indicating a low discrepancy between both models. Besides, after the thermal arrest the curve calculated with model B lies above the one calculated with model L but towards the end of the cooling process they finally superpose. Regarding Si segregation and liquid fraction evolution both models predict very similar tendencies with little differences towards the end of the cooling process, between 200 and 350 s. On the other hand, when comparing the final nodule count obtained with both models a small difference is appreciated. This difference is about 35% in classes 1. Model L, unlike model B, predicts the presence of nodules in class 3. On the other hand, model B, unlike model L, predicts the presence of nodules in class 4.

Taking into account these results, the next stage is to implement both models in a more complex configuration, i.e. a wedge-like part in this study. These results are presented in the following section ‘Analysis of wedge-like part’.

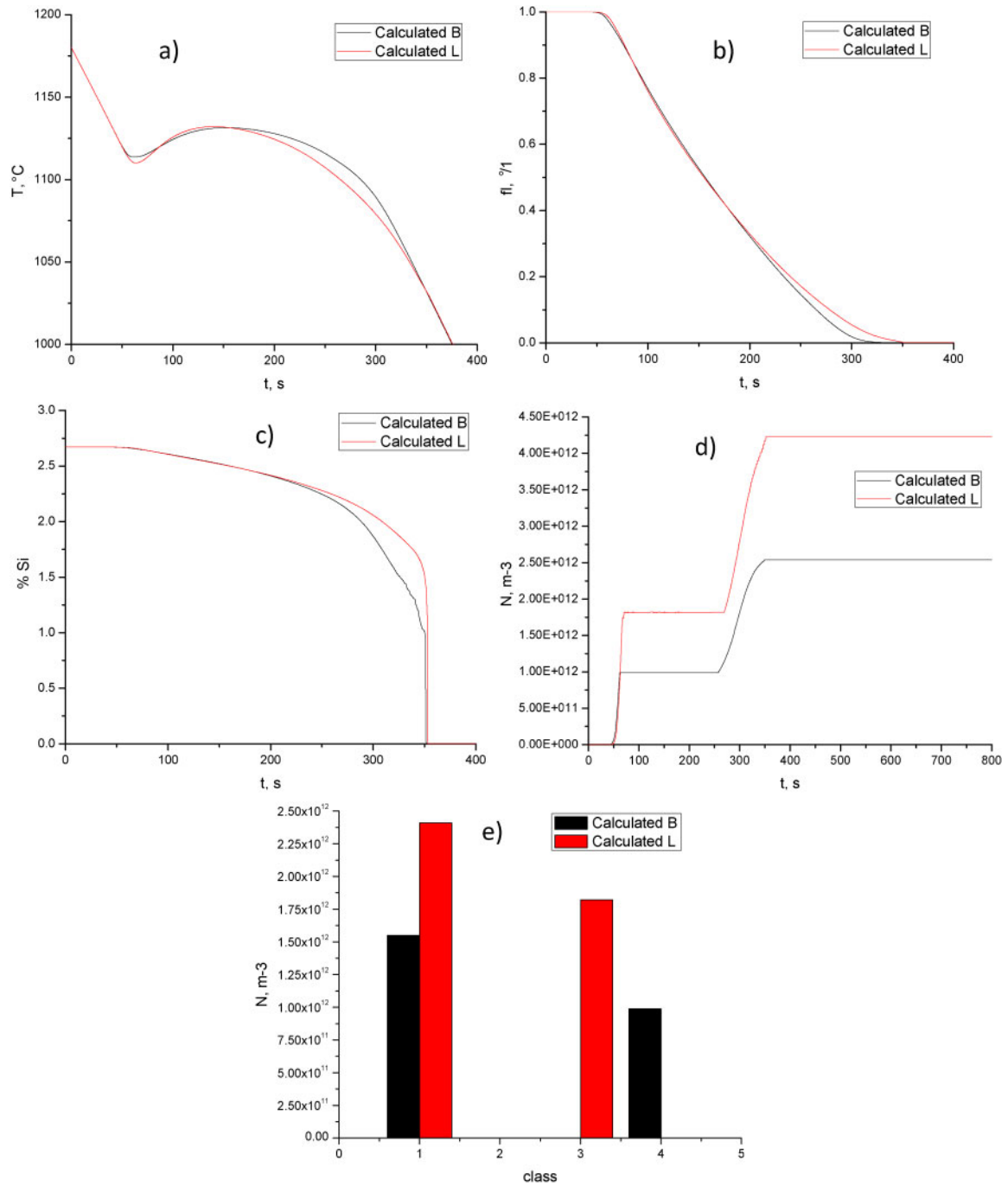
Analysis of wedge-like part

In order to analyse the cooling process of the cast and mould in a wedge-like part, the multinodular and uninodular models presented in the section ‘Numerical modelling’ and first compared in the previous section were used. The results of such models are separately described and discussed below.

To achieve an acceptable numerical–experimental fit with model B, an error analysis was firstly necessary. This analysis was made varying the nucleation parameters in equation (11) of Table 4 and calculating the

Table 7 Thermal properties of the interfaces²⁰

| Interface | Heat transfer coefficient/W m ⁻² °C ⁻¹ |
|---------------|--|
| Mould/air | 50 |
| Casting/air | 70 |
| Casting/mould | 3000 |



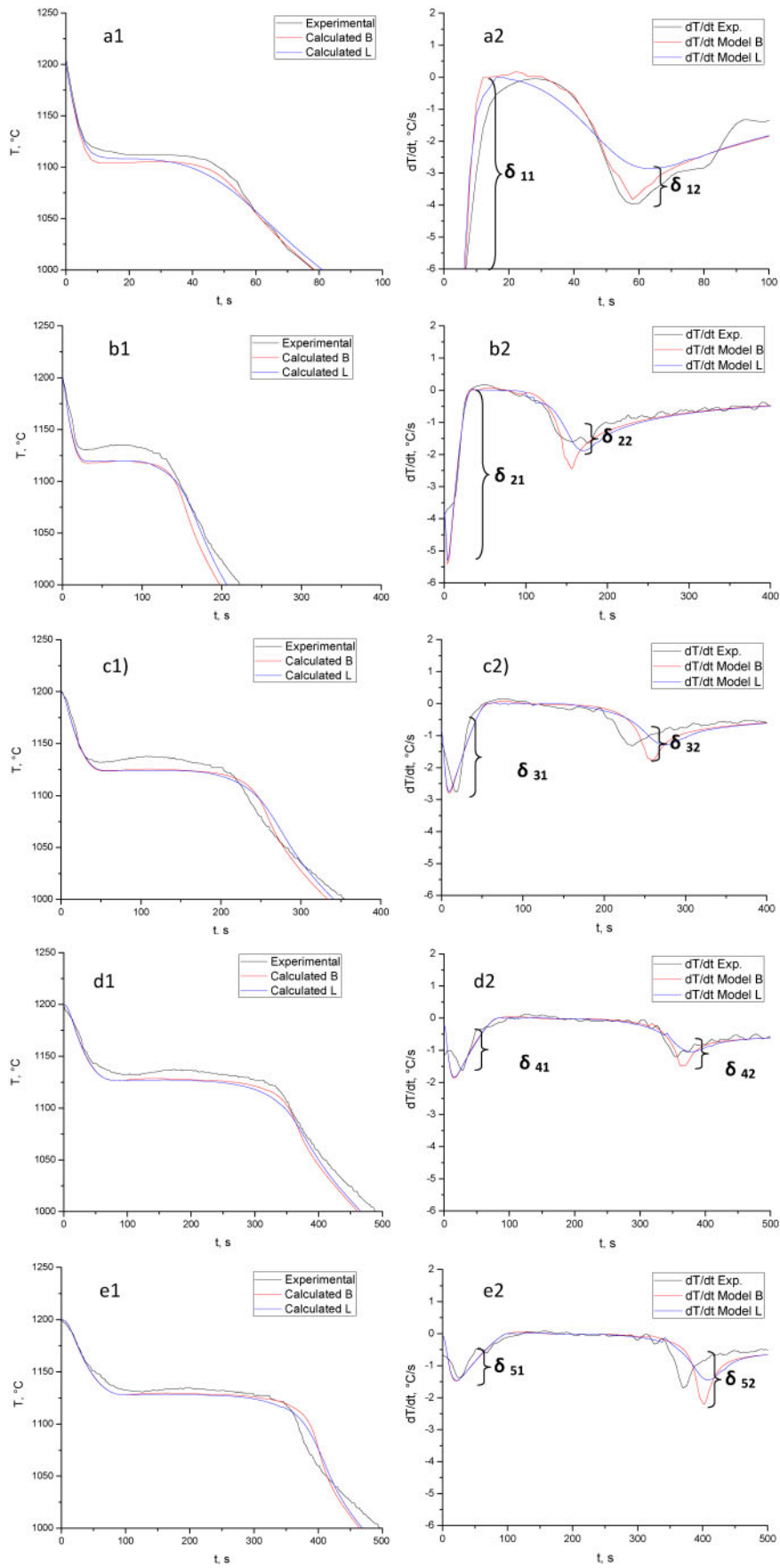
a cooling curve; b liquid fraction evolution; c Si evolution; d nodule count evolution; e final nodule count
3 1D numerical simulation comparing models B and L

discrepancy between the numerical and the experimental results via the application of a standard least squares minimisation technique for all the variables considered in the analysis. After this long stage, a very satisfactory fit was obtained. The derived parameters are shown in Table 5.

In Fig. 4 the experimental and calculated cooling and cooling rate curves for thermocouples at the five locations analysed are shown. It is appreciated in Fig. 4a2-e2 that, especially in the first stage of the cooling process, as thickness increases (from T1 to T5) the cooling rate decreases as expected. This is accounted by the parameter δ_{ij} ($i=1, 2, \dots, 5; j=1, 2$) which represents the change in the cooling rate imposed in each point of the wedge. Accordingly, there is a

continuous increase in the experimental and numerical solidification time of the points located at the different places of the wedge-like part. Those located in the thicker parts show a longer solidification time than the ones located in the thinner parts thus showing the metal thickness effect on the cooling process. These values are presented in Table 8. In this table it is shown that the experimental nodule count, despite the value in T3, increases as cooling rate increases. This is well predicted by both models which also overestimate the number of nodules per unit volume in location T5.

In all the positions of the wedge-like part the numerical simulation of the cooling process obtained with model B predicted a very similar solidification time than that obtained experimentally. As also can be seen,



a T1; b T2; c T3; d T4; e T5

4 Experimental and calculated cooling and cooling rate curves obtained with models B and L at positions

Table 8 Experimental and numerical nodule count and solidification time at locations T1–T5

| Location | N_V/m^{-3} (Exp.) | N_V/m^{-3} (Model B) | N_V/m^{-3} (Model L) | T_F/s (Exp.) | T_F/s (Model B) | T_F/s (Model L) |
|----------|-----------------------|------------------------|------------------------|----------------|-------------------|-------------------|
| T1 | 2.29×10^{13} | 1.06×10^{13} | 1.36×10^{13} | 56.2 | 57.6 | 63.1 |
| T2 | 8.75×10^{12} | 9.19×10^{12} | 1.27×10^{13} | 178.3 | 156.3 | 170.0 |
| T3 | 1.02×10^{13} | 7.87×10^{12} | 1.14×10^{13} | 252.3 | 258.6 | 274.2 |
| T4 | 8.86×10^{12} | 6.45×10^{12} | 9.56×10^{12} | 354.2 | 366.7 | 379.3 |
| T5 | 8.58×10^{12} | 7.89×10^{12} | 1.12×10^{13} | 375.9 | 402.1 | 407.8 |

in all the positions the numerical curves lie below the experimental ones. The bulk eutectic reaction temperature is not as well predicted by models B and L in locations T1–T3 as in locations T4 and T5. Besides, although in all the locations the numerical and experimental thermal arrests are slightly different in temperature, they are very similar in the time extension, especially in locations T4–T5. At the end of the solidification process, the slopes of the experimental and numerical cooling curves are very similar, i.e. in general a good numerical–experimental fit was obtained. To this point we may conclude that the numerical–experimental fit achieved with model B improves for the thicker parts of the sample.

When comparing the numerical results obtained with models B and L it can be seen that the solidification time and the characteristic temperatures of the cooling process calculated with both models are very similar for all the positions of the sample. Unlike the other locations, in location T1 before and after the eutectic reaction the curve obtained with model L lies above the one obtained with model B. In locations T2–T5 both curves practically superpose most of time but towards the end of the cooling process they slightly separate. When comparing these results with the experimental ones it can be seen that both models reproduce very well the cooling process of the analysed sample. This can be especially appreciated in Fig. 4b–e, where the numerical cooling curves show the same arrest temperature. In addition, at the end of the solidification process the slope of the numerical (obtained with models B and L) and experimental curves are very similar in all the locations analysed.

Figure 5 shows the as cast microstructures obtained in locations T1–T5. Micrographs in the right column were taken in the same position and etched with 3% nital. As can be seen there is a continuous growth of the graphite nodules, from the thinner (T1) to the thicker parts (T5) of the samples, because of the effect of cooling rate on the nucleation and growth time of a nodule during the solidification process. As shown in Fig. 5a2, the presence of seldom carbides distributed randomly in the structure was revealed in location T1. When compared to the others locations (T2–T5) it is seen that the carbide phase is not present any longer. In these locations the microstructure is composed mainly by varying amounts of pearlite, ferrite and graphite nodules. Accordingly, there is a change in the graphite fraction when comparing the microstructure of location T1 with the rest of them because part of the carbon is present in the form of the carbide phase (metastable phase) and thus, by balance, this situation gives a lower fraction of the stable phase.

Figure 6 shows the experimental and calculated (with models B and L) nodule density (N_V) obtained at locations T1–T5. As can be appreciated, in all the

locations there exist a difference between the experimental and calculated nodule sizes and distributions of nodules in the matrix. In each location the bigger differences were found to be in the smaller classes of the distribution, especially in class 1. In general, in all the locations a very similar tendency can be seen both numerically and experimentally, meaning that in both cases there are mainly small nodules. When comparing the numerical models it can be seen that in all the locations model L shows a bigger numerical–experimental discrepancy in the volume nodule count for class 1 than model B.

As presented above, an important stage of the present study was to compare the numerical results obtained with models B and L. It is seen in Figs. 4 and 6 that the results obtained with the two models are very similar in terms of cooling curves and nodule count. At the first and final stages of the cooling process, the slope of the curves is almost the same. The start of the eutectic reaction, in time scale, is almost the same. The cooling process predicted by model B takes only a little shorter time compared to the one predicted by model L, thus indicating the high similarity between these two models. As shown above, this is what also occurs experimentally in all the samples. According to these results we can conclude that both theories, uninodular and multinodular, show a very similar tendency when describing the solidification process of a SGI with eutectic composition.

Conclusions

Multinodular based and uninodular based models were used to simulate the cooling process of an eutectic spheroidal graphite cast iron and it was experimentally validated. From the realisation of this work the following conclusions can be drawn:

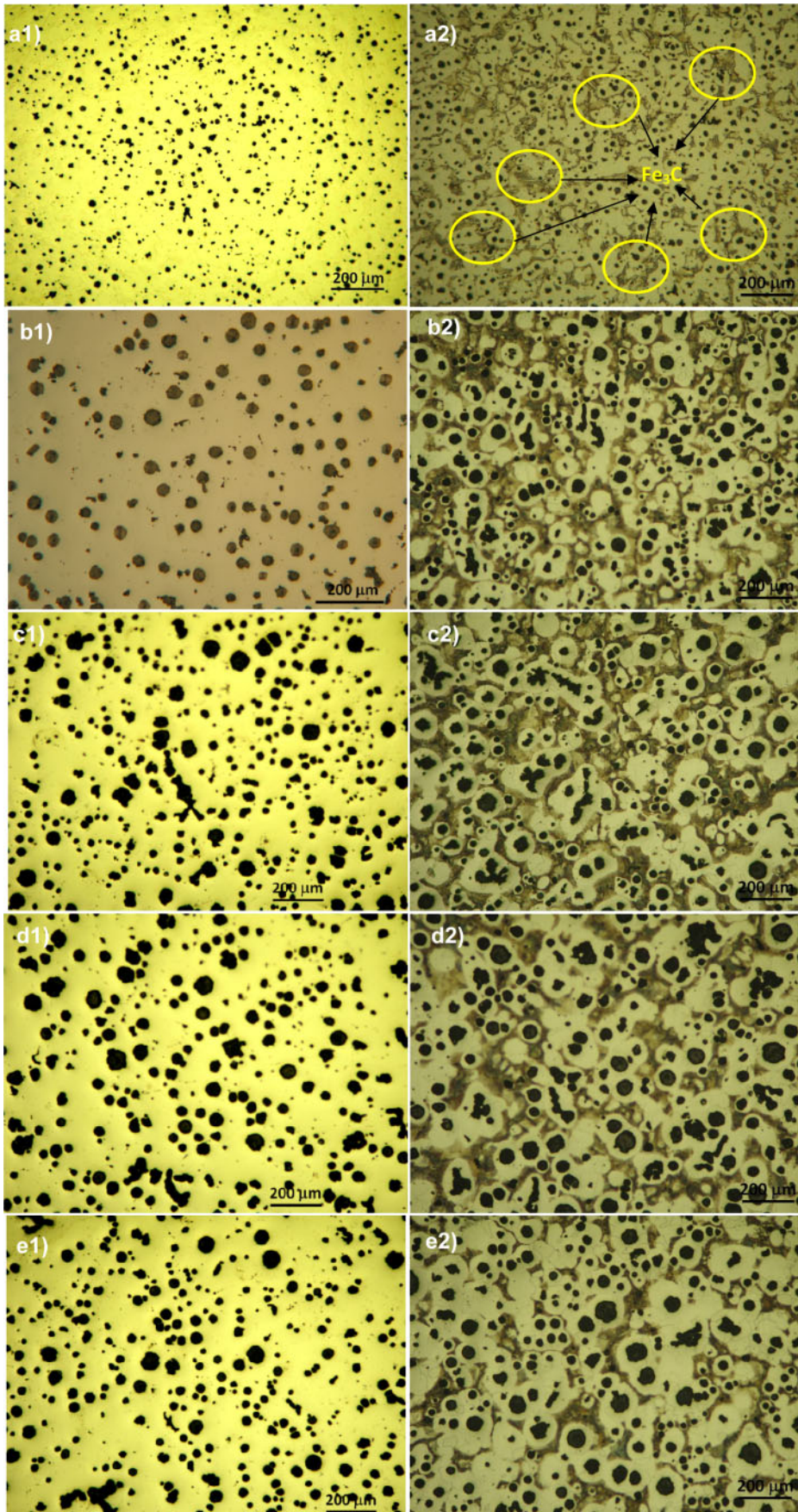
in the thinner parts of the sample (positions T1 and T2) the model predicts a lower temperature for the eutectic reaction to proceed and a longer solidification time than experiments.

A satisfactory and very good agreement was obtained between the experimental data and the numerical simulations of the solidification process, especially for the thicker parts of the castings.

It was experimentally and numerically shown that as thickness increases the cooling rate decreases, as accounted by the parameter δ .

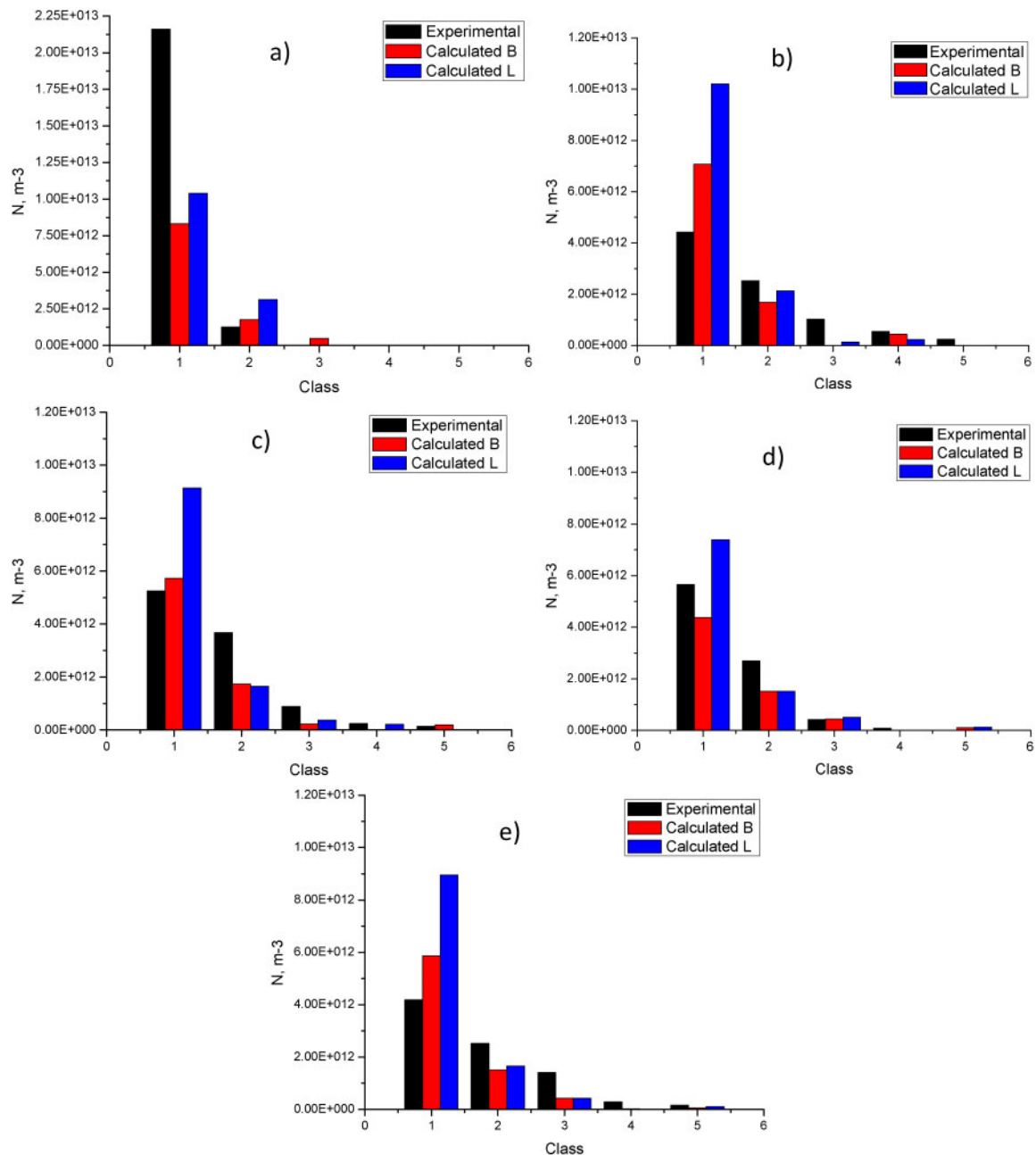
From the present work it is assumed that it is possible to understand and potentially achieve a better control of the cooling rate effect on the final microstructure of a nodular cast iron.

The experimental nodule density was, in general, in good agreement with the simulated ones. The larger differences are found to be in location T1 which can be related to the higher cooling rates of these points and the



a1, a2 T1; b1, b2 T2; c1, c2 T3; d1, d2 T4; e1, e2 T5

5 As cast microstructures at positions



a T1; b T2; c T3; d T4; e T5

6 Experimental and numerical nodule count obtained with models B and L at positions

low capability of the models to reproduce satisfactorily what occurs at these points.

The comparison of the results obtained with the multinodular model (Model B) and the ones obtained with a uninodular based model (Model L) shows a good agreement with each other.

The comparison of models B and L was useful to confirm that both uninodular and multinodular models of growth can be used to analyse and study the solidification process of an eutectic spheroidal graphite cast iron taking into account the postulates of each one.

Acknowledgements

The first author of this work thanks the financial support given by CONICYT (Chilean Council of Research and Technology) for the realisation of it and of an internship carried out in Toulouse (ENSIACET),

France. The authors also thank CONICYT for the support provided by Project Fondecyt 1130404. A particular acknowledgement goes to José Miguel Zúñiga, co-owner of TECNOMETAL, for his support in the experimental stage of this work.

References

1. Sorelmetal: Ductile Iron Data for Design Engineers, Rio Tinto Iron & Titanium Inc., Canada, 1990.
2. M. Ashraf Sheikh: 'Production of carbide-free thin ductile iron castings', *J. Univ. Sci. Technol. Beijing*, 2008, **15**, 552.
3. D. M. Stefanescu: 'Science and engineering of casting solidification'; 2002, New York, Kluwer Academic/Plenum Publishers.
4. B. Lux, F. Mollard and I. Minkoff: in 'The metallurgy of cast iron', (ed. B. Lux *et al.*), 371; 1975, St. Saphorin, Georgi Publishing Co.
5. H. Jones and W. Kurz: *Metall. Trans. A*, 1980, **11A**, 1265.
6. S. Wetterfall, H. Fredriksson and M. Hillert: *J. Iron Steel Inst.*, 1972, **210**, (Pt I), 323–332.

7. K.C. Su, I. Ohnaka, I. Yamauchi and T. Fukusako: Proc. 3rd Int. Symp. on 'Physical metallurgy of cast iron', 181–189; 1985, New York, North-Holland.
8. G. Lesoult, M. Castro and J. Lacaze: *Acta Mater.*, 1998, **46**, 983–995.
9. J. Lacaze, M. Castro and G. Lesoult: *Acta Mater.*, 1998, **46**, 997–1010.
10. M. Rappaz, J. D. Richo and Ph. Thévoz: Euromat 89, E-MRS, Aachen-RFA, 1989, 1–6.
11. M. Castro, P. Alexandre, J. Lacaze and G. Lesoult: Proc. 'Cast Iron IV' Conf., 1989, Tokyo, Japan. 433; 1990, Materials Research Society.
12. E. Fras, W. Kapturkiewicz and A. Burbielko: in 'Modelling of casting, welding and advanced solidification processes VII', (ed. M. Cross and J. Campbell), 679–686; 1995, Warrendale, PA, The Minerals, Metals and Material Society.
13. J. Liu and R. Elliot: *J. Crystal Growth*, 1998, **191**, 261–267.
14. E. Fras: Proc. 3rd Int. Symp. on 'Physical metallurgy of cast iron', 191–199; 1985, New York, North-Holland.
15. H. Fredriksson and I. Svensson: Proc. 3rd Int. Symp. on 'Physical metallurgy of cast iron', 273–284; 1985, New York, North-Holland.
16. D. M. Stefanescu and C. S. Kanetcar: 'Computer simulation of microstructural evolution', (ed. O. J. Srolovitz), 171–188; 1986, New York, TMS-AIME.
17. G. Rivera, R. Boeri and J. Sikora: *Int. J. Cast Met. Res.*, 1999, **11**, 267–272.
18. R. Boeri: 'The solidification of ductile cast iron', PhD thesis, The University of British Columbia, 1989.
19. D. J. Celentano, P. M. Dardati, L. A. Godoy and R. Boeri: *Int. J. Cast Met. Res.*, 2008, **21**, (6), 416–426.
20. P. M. Dardati, D. J. Celentano, L. A. Godoy, A. A. Chiarella and B. J. Schulz: *Int. J. Cast Metals Res.*, 2009, **22**, 390–400.
21. P. M. Dardati, L. A. Godoy and D. J. Celentano: *ASME J. Appl. Mech.*, 2006, **73**, (6), 977–983.
22. W. Oldfield: *Trans. Of ASM*, 1966, **59**, 945.
23. J. Lacaze: *Acta Mater.*, 1999, **47**, 3779–3792.
24. C. Selig and J. Lacaze: *Metall. Trans. B*, 2000, **31B**, 827–836.
25. T. Owadano: 'Graphite nodule number in spheroidal graphite and malleable cast irons', *ImonolJapan Foundr. Soc.*, 1973, **45**, 193–197.
26. C. B. Basak and A. K. Sengupta: 'Development of a FDM based code to determine the 3D size distribution of homogeneously dispersed spherical second phase from microstructure: a case study on nodular cast iron', *Scr. Mater.*, 2004, **51**, 255–260.
27. R. W. Heine: *AFS Trans.*, 1986, **71**, 391–402.
28. D. J. Celentano: 'Un Modelo Termomecánico para Problemas de Solidificación de Metales', PhD thesis, Polytechnic University of Catalunya, Barcelona, 1994.
29. D. J. Celentano, S. Oller and E. Oñate: *Int. J. Solids Struct.*, 1996, **33**, (5), 647–673.